INSTITUTE OF PHYSICS PUBLISHING MEASUREMENT SCIENCE AND TECHNOLOGY
Meas. Sci. Technol. **13** (2002) 683–694 PII: S0957-0233(02)26851-4

Defocusing digital particle image velocimetry and the three-dimensional characterization of two-phase flows

Francisco Pereira[1] **and Morteza Gharib**

Center for Quantitative Visualization, Graduate Aeronautical Laboratories, California Institute of Technology, Pasadena, CA 91125, USA

E-mail: frisco@caltech.edu

Received 12 July 2001, in final form 14 February 2002, accepted for publication 1 March 2002
Published 28 March 2002
Online at stacks.iop.org/MST/13/683

Abstract
Defocusing digital particle image velocimetry (DDPIV) is the natural extension of planar PIV techniques to the third spatial dimension. In this paper we give details of the defocusing optical concept by which scalar and vector information can be retrieved within large volumes. The optical model and computational procedures are presented with the specific purpose of mapping the number density, the size distribution, the associated local void fraction and the velocity of bubbles or particles in two-phase flows. Every particle or bubble is characterized in terms of size and of spatial coordinates, used to compute a true three-component velocity field by spatial three-dimensional cross-correlation. The spatial resolution and uncertainty limits are established through numerical simulations. The performance of the DDPIV technique is established in terms of number density and void fraction. Finally, the velocity evaluation methodology, using the spatial cross-correlation technique, is described and discussed in terms of velocity accuracy.

Keywords: two-phase flow velocity, size distribution, void fraction, particle image velocimetry, light scattering, dynamic surface mapping

1. Introduction

Since its appearance in the 1970s, particle image velocimetry (PIV) has gained an increasingly important role in experimental fluid mechanics. PIV systems are nowadays commercially available to a broad scientific community.

PIV is part of a whole class of velocity measuring techniques including laser speckle velocimetry (LSV) (Meynart 1983), planar laser induced fluorescence (Gharib *et al* 1985), nuclear magnetic resonance (Lee *et al* 1987), particle tracking velocimetry (Racca and Dewey 1988), molecular tagging velocimetry (Miles *et al* 1989) and others. The primary advantage of PIV over single-point measurement techniques such as hotwire anemometry and laser Doppler anemometry, is its ability to provide global, non-intrusive and spatially highly resolved measurements of planar velocity vector fields (Adrian 1986), though with a lower temporal resolution. The velocities are obtained by determining the displacements of flow markers using correlation techniques (Kimura and Takamori 1986). The term PIV is usually applied when the concentration of markers lies between the high densities needed for LSV and the lower concentrations found in particle tracking velocimetry (PTV). For a long time, highly resolved PIV photographs were the common way to record the flow field. The technique naturally evolved to digital recording when electronic components such as charge coupled devices (CCD) became commercially available (Cho 1989, Willert and Gharib 1991). Accordingly, the theory for PIV interrogation by correlation algorithms (Keane and Adrian 1992) was updated to account for this recording evolution (Westerweel 1997).

However, the technique and theory remained inherently confined to planar domains, for features present in highly

[1] Author to whom any correspondence should be addressed.

turbulent or unsteady flows could not be captured in their full integrity. To address this issue, efforts have been made to extend the spatial range of measurement of PIV to the third spatial dimension. Ingenious set-ups have been implemented to extract the so-called out-of-plane component from combined planar views of the flow field: angular (Gauthier and Riethmuller 1988), translational (Prasad and Adrian 1993), single camera setup (Reese *et al* 1995), Scheimpflug arrangement (Prasad and Jensen 1995), in-line (Grant *et al* 1995), multilayer (Raffel *et al* 1996, Abe *et al* 1998), scanning (Brücker 1997), multiplane (Kähler and Kompenhans 2000).

Existing true three-dimensional (3D) techniques are still seldom used because of their technical complexity combined with their limited spatial and/or temporal resolution. Holographic techniques such as HPIV are the most noticeable, praised for their high potential but reluctantly implemented due to their delicate optical set-up and sensitivity to environment perturbations. The optical reconstruction of the 3D field from the recorded hologram allows a post-interrogation by techniques such as microscopic photography, PIV or PTV. Katz *et al* (1983) were among the first to use a holographic system for fluid research; using a microscope to scan the reconstructed hologram, the population and size distributions of cavitation nuclei in a water tunnel were obtained. To minimize the sensitivity to speckle noise and to improve the scattering efficiency, Zhang *et al* (1997) devised a novel configuration to perform turbulent flow measurement in a square duct and used PIV to interrogate the hologram. HPIV systems have also been shown to be implementable in field situations (Malkiel *et al* 1999). However, the interrogation process of the holograms is a time-consuming operation and still relies for a large part upon the human supervision, even though automatic procedures have been developed (Green and Zhao 1994).

PIV provides an Eulerian representation of the flow physical descriptors. In contrast, the PTV technique is a true 3D approach providing a more natural description known as Lagrangian representation (Malik and Dracos 1993). PTV derives from traditional flow visualization techniques such as streak photography, and is based on the coordinate determination by triangulation and on the tracking of individual markers, such as bubbles or neutrally buoyant seeding tracers (Sheu *et al* 1982). Particle tracking is usually applicable under two restrictive conditions. Firstly, the concentration of scatterers must be low to perform a reliable identification. With large densities, ambiguities arise and tracks cannot be reconstructed correctly, unless redundant information is made available by additional recording cameras. Secondly, the displacements, or tracks, must be small enough compared with the mean spacing between the particles (Adrian 1991). Hence, if PTV overcomes the incapacity of PIV to follow the motion of particles, this is done at the price of a lower spatial resolution for the velocity field. In addition, the photogrammetric determination of the particle coordinates requires a thorough calibration of the camera system (Murai *et al* 1980). PTV is now at a stage where implementation can be achieved with reasonable effort and is largely documented (Agüí and Jiménez 1987, Nishino *et al* 1989).

The defocusing digital PIV (DDPIV) technique, the foundations of which have been established in an early work by Willert and Gharib (1992), is a new approach to the 3D mapping of flow fields. The interrogation domain is a volume where 3D coordinates of fluid markers are determined prior to flow analysis. However, unlike PTV or stereo-based methods, DDPIV has one unique optical axis and is based on pattern matching rather than on stereoscopic matching of particle images. The other fundamental difference resides in the statistical evaluation of the particle displacement, which is here recovered by performing a 3D spatial correlation of particle locations. In that sense, DDPIV uses the same methodology as planar DPIV does in the pixel domain of the particle images. Terms such as single-frame double or multiple exposure, or multi-frame single exposure are still fully applicable, except that the DDPIV frame is here represented by a volumetric ensemble of particles. The purpose of this paper is to provide an extensive layout of the DDPIV fundamentals. In the first part, we detail the principle of the defocusing technique and provide the geometrical definitions that undergo the optical design of a defocusing system. An uncertainty analysis is developed to provide a comparison basis with other systems. In the second part, the computational implementation of the pattern matching approach is laid out. Using a simple computer model, the performance of the DDPIV method is numerically assessed in terms of spatial errors and of the particle size and number distributions. The last part describes the theory as well as the computational implementation of the 3D spatial cross-correlation used to determine the velocity, concluded by a parametric study of the displacement errors induced by this procedure.

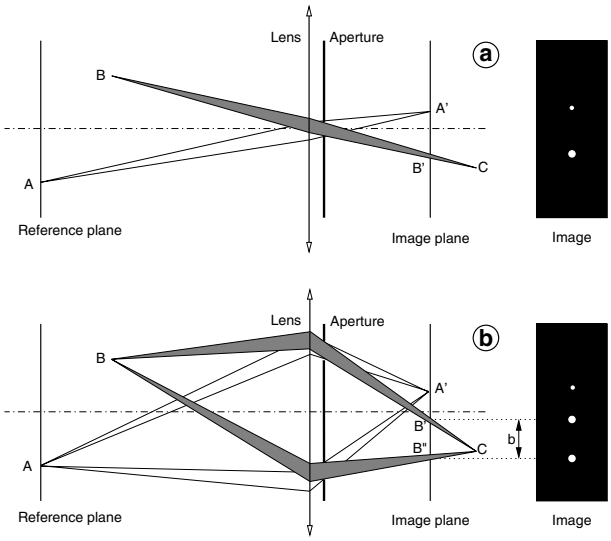

Figure 1. The defocusing principle: (*a*) standard imaging system, (*b*) defocusing arrangement.

2. Defocusing concept

For clarity, we use the generic term 'particle' for a solid particle, a gas bubble or a liquid droplet.

2.1. Principle

A typical two-dimensional (2D) imaging system, consisting of a converging lens and of an aperture, is represented in

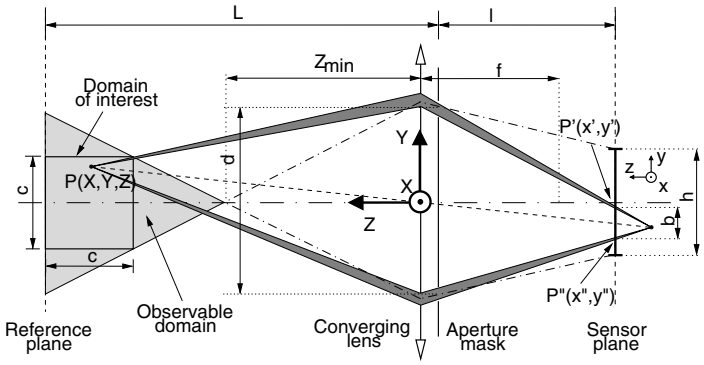

Figure 2. Simplified defocusing optical model.

figure 1(*a*) to help describe the DDPIV technique. The point A, located on the object plane (or reference plane), appears focused as A′ on the image plane (or sensor plane). The point B located in between the reference plane and the lens system is projected as a blurred image B′.

The DDPIV technique uses a mask with two or more apertures shifted away from the optical axis to obtain multiple images from each scattering source, as shown in figure 1(*b*) with the images B′ and B″ of point B. The image shift b on the image plane, caused by these off-axis apertures, is related to the depth location of the source points.

2.2. Geometrical analysis

A simplified geometrical model of a two-aperture defocusing optical arrangement is represented in figure 2. The domain of interest is defined by a cube of side c. The far face of this cube is coplanar with the reference plane at a distance L from the lens plane. Let d be the distance between apertures (or pinholes), f the focal length of the converging lens and l the distance from the lens to the image plane, materialized by a photosensor (e.g. CCD) with height h. The physical space is attached to a coordinate system originating in the lens plane, where the Z-axis corresponds to the optical axis of the system; the coordinates are (X, Y, Z). The image coordinate system is the Z-translation of the physical system onto the sensor plane, i.e. at $Z = -l$. The coordinates of a pixel on the imaging sensor are given by the pair (x, y). Point $P(X, Y, Z)$ represents a light scattering source. For $Z \neq L$, P is projected onto points P' and P'', separated by the distance b.

The cubic domain defined by c is a design constraint: the observable and measurable domain is in fact a volume that extends from the reference plane to a location on the optical axis with coordinates $(0, 0, Z_{min})$, see figure 2. Any particle present in this volume is imaged on the sensor by two distinct images separated by the distance b, except for $Z = L$ where $b = 0$. Z_{min} is given by

$$Z_{min} = \frac{d(L-c)}{c+d}. \tag{1}$$

Image coordinates. (x', y') and (x'', y'') are the image coordinates of P' and P'' in the image plane

$$\begin{aligned} x' &= x'' = -ML\frac{X}{Z} = -M_Z X \\ y' &= \frac{M}{2Z}[d(L-Z) - 2LY] \\ y'' &= \frac{M}{2Z}[-d(L-Z) - 2LY] \end{aligned} \tag{2}$$

where M is the nominal optical magnification provided by the lens equation and M_Z is the Z-related magnification factor:

$$M = \frac{f}{L-f}, \qquad M_Z = M\frac{L}{Z}. \tag{3}$$

In practice, the size h of the photosensor, the size c of the interrogation volume and the focal distance L are specific to the application. Instead, f and d are chosen so that the optical magnification M equals the geometrical magnification imposed by h, c and L. Therefore, M should also comply with the relation

$$M = \frac{h\,(L-c)}{c\,(L+d)}. \tag{4}$$

Image separation. The image separation vector $\boldsymbol{b}$ represents the distance between P' and P''. The norm is given by

$$\begin{aligned} b &= d\,|M_Z - M| \\ &= \frac{1}{K}\left|\frac{1}{Z} - \frac{1}{L}\right| \qquad \text{with } K = \frac{1}{MdL} \end{aligned} \tag{5}$$

b is reported in figure 3 versus the ratio Z/L, and is non-dimensionalized by the height h of the imaging sensor. b/h is equal to zero for $Z = L$ and equals unity for $Z = Z_{min}$. Three values of d are considered for the aperture separation, equations (3) and (4) providing the adequate focal lengths f. The sizelength c of the cubic interrogation domain is set to 100 mm and the focal distance is $L = 1000$ mm.

Equation (5) demonstrates the extreme simplicity of the defocusing concept: (1) the image separation b is not a function of the coordinates X and Y; (2) the aperture diameter has no bearing on b and is only responsible for the amount of blur and incident intensity. However, these observations are only valid if the system is free of optical aberrations, which is our assumption here. In practice, a careful optical simulation is an absolute prerequisite to assess and minimize the focusing aberrations, whereas image distortions can be compensated through calibration procedures (Soloff *et al* 1997).

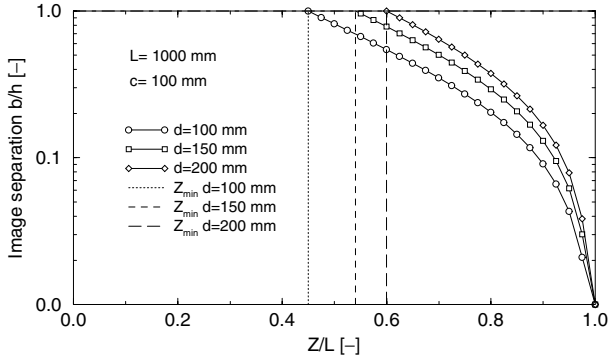

Figure 3. Image separation b.

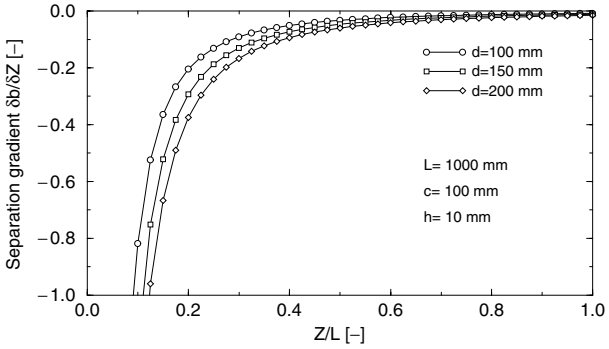

Figure 4. Image separation gradient $\partial b/\partial Z$.

$\boldsymbol{b}$ changes sign across the plane $Z = L$. In other terms, the image pattern defined by the image pair P' and P'' inverts orientation when the object point P crosses the reference plane. For a two-aperture design as depicted in figure 2, this result leads to a non-uniqueness problem because b, as defined by equation (5), is a monotonically decreasing function in the interval $[0, L]$. To overcome this ambiguity, one can either use distinct shapes for the apertures or use multiple apertures. In a prototype DDPIV instrument, Pereira *et al* (2000) used a mask with three pinholes forming a triangular pattern, which inverts its orientation when P moves across the reference plane.

The sensitivity of the system, i.e. its ability to detect small changes of the particle location, can be evaluated through the separation gradient

$$\frac{\partial b}{\partial Z} = -\frac{1}{KZ^2}. \tag{6}$$

$\partial b/\partial Z$ is independent of the components X and Y. This gradient is reported in figure 4 versus Z/L for different distances d between apertures, using the same values of L and c as above and with $h = 10$ mm. The plots show that the sensitivity increases with d. In practice, however, and for the same experimental configuration, this improvement is only partially affordable: the system f-number is lowered to prohibitive levels because of the larger size of the converging lens.

Space coordinates. The coordinates of P in the coordinate system attached to the camera are derived from the image coordinates of the projections P' and P'':

$$\begin{aligned} X &= -\frac{x_0}{M_Z} \qquad \text{with } x_0 = \frac{x' + x''}{2} \\ Y &= -\frac{y_0}{M_Z} \qquad \text{with } y_0 = \frac{y' + y''}{2} \\ Z &= \left(\frac{1}{L} + Kb\right)^{-1}. \end{aligned} \tag{7}$$

Assuming that the apertures are equidistant from the origin of the coordinate system, the image point defined by (x_0, y_0) is the image of the particle if there is a single aperture at the origin.

2.3. Uncertainty analysis

Let the vectors $\boldsymbol{dP}'(\mathrm{d}x', \mathrm{d}y')$ and $\boldsymbol{dP}''(\mathrm{d}x'', \mathrm{d}y'')$ be the infinitesimal displacements on the image sensor plane of P' and P'', and $\boldsymbol{dP}(\mathrm{d}X, \mathrm{d}Y, \mathrm{d}Z)$ the infinitesimal displacement in the object space coordinate system of object point P. The total partial differential of any variable ζ is defined by

$$\mathrm{d}\zeta = \frac{\partial \zeta}{\partial X}\mathrm{d}X + \frac{\partial \zeta}{\partial Y}\mathrm{d}Y + \frac{\partial \zeta}{\partial Z}\mathrm{d}Z. \tag{8}$$

Differentiating P' and P'' in terms of X, Y and Z leads to the infinitesimal particle image displacements $(\mathrm{d}x', \mathrm{d}y')$ and $(\mathrm{d}x'', \mathrm{d}y'')$

$$\begin{pmatrix} \mathrm{d}x' \\ \mathrm{d}y' \\ \mathrm{d}x'' \\ \mathrm{d}y'' \end{pmatrix} = \begin{pmatrix} A & 0 & B \\ 0 & A & C \\ A & 0 & B \\ 0 & A & D \end{pmatrix} \cdot \begin{pmatrix} \mathrm{d}X \\ \mathrm{d}Y \\ \mathrm{d}Z \end{pmatrix} \tag{9}$$

where

$$\begin{aligned} A &= -\frac{ML}{Z}, \qquad & C &= -\frac{MdL}{2Z^2} + \frac{MLY}{Z^2} \\ B &= \frac{MLX}{Z^2}, \qquad & D &= \frac{MdL}{2Z^2} + \frac{MLY}{Z^2}. \end{aligned} \tag{10}$$

Let us assume that the uncertainties in the geometric parameters f, d and L are negligible. We assume also that the position of the particle image centroid can be measured with an equal error Δx. This assumption holds if the apertures of the system are small compared with the focal length f, thus extending the optical depth-of-field so as to cover the full working domain, from $Z = Z_{min}$ to L. If this condition is not respected, the size of the particle image increases due to blurring with the inverse of Z and with the diameter of the apertures, and so does the uncertainty on the centroid location of the particle image on the sensor. Under the above constraint,

$$\delta(\mathrm{d}x') = \delta(\mathrm{d}y') = \delta(\mathrm{d}x'') = \delta(\mathrm{d}y'') = \Delta x. \tag{11}$$

After inversion of the matrix equation (9), the uncertainties on the object space displacements $(\mathrm{d}X, \mathrm{d}Y, \mathrm{d}Z)$ can be derived using standard error procedures:

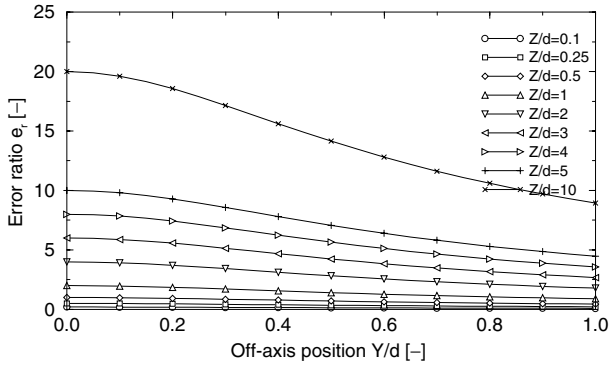

Figure 5. Error ratio e_r versus the off-axis position Y/d, for different distances to camera Z/d.

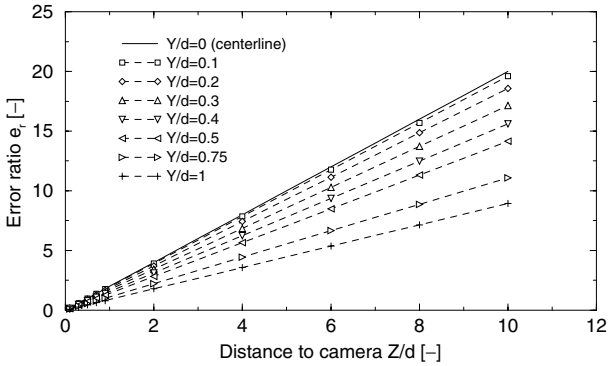

Figure 6. Error ratio e_r versus the distance to camera Z/d, for different off-axis positions Y/d.

$$\delta(\mathrm{d}X) = \Delta x \frac{\sqrt{(C-D)^2+2B^2}}{|A(C-D)|} = K\,\Delta x |Z| \sqrt{d^2+2X^2}$$
$$\delta(\mathrm{d}Y) = \Delta x \frac{\sqrt{C^2+D^2}}{|A(C-D)|} = K\,\Delta x |Z| \sqrt{\frac{d^2}{2}+2Y^2}$$
$$\delta(\mathrm{d}Z) = \Delta x \frac{\sqrt{2}}{|C-D|} = K\,\Delta x Z^2 \sqrt{2}. \tag{12}$$

From equation (6), we can write

$$\delta(\mathrm{d}b) = \sqrt{2}\,\Delta x. \tag{13}$$

The uncertainty on X is distinct from that on Y because of the particular aperture geometry of our model, see figure 2, for the definition of the image coordinates (x', y') and (x'', y'') of equations (2) depend on the aperture arrangement. $\delta(\mathrm{d}X)$ and $\delta(\mathrm{d}Y)$ are found to depend linearly upon the Z-component and the respective X or Y component. The minimum errors for the transversal and vertical components are reached on the optical axis. $\delta(\mathrm{d}Z)$ depends quadratically on Z and is constant in any plane orthogonal to the optical axis.

A measure of the overall performance of the system can be represented by the ratio between the individual error components. This provides dimensionless terms that can be used as a comparison criterion between different techniques or as a guide criterion in the design stage in order to meet the resolution requirements. In planar PIV techniques, the depth component is derived from in-plane information. For this reason, the ratio between the out-of-plane and the in-plane error components is a first choice (see, for example, Prasad and Adrian 1993). Using the same approach, let e_r be the ratio $\delta(\mathrm{d}Z)/\delta(\mathrm{d}Y)$, this case presenting the less favourable situation:

$$e_r = \frac{|Z|}{d\,\sqrt{(1/4)+(Y/d)^2}}. \tag{14}$$

e_r depends exclusively on one geometrical parameter: the distance d between apertures. e_r is reported in figure 5 as a function of the off-axis position Y/d, for different distances Z/d. e_r is maximum at and symmetrical about the centreline ($Y/d = 0$), and falls away from the centre of the field. Figure 6 shows e_r versus Z/d and for various values of the off-axis position Y/d. For a given aperture distance d and a given off-axis position, e_r varies linearly with distance Z.

3. Particle 3D location

3.1. Particle image detection

We assume that the particle field is recorded and digitized into 2D discrete arrays of pixels. These images are, in a first stage, preprocessed by classical image processing operators: background removal; intensity normalization; definition of regions of interest; low-pass filtering.

The second stage performs a fast detection of local peaks. Although local peak detection techniques are common in image processing literature (Higuchi *et al* 1994), a new algorithm is proposed to overcome the practical problems of particle overlapping, residual background noise and non-uniformity of illumination. The algorithm has the ability to reliably discriminate spherical from non-spherical particles. Every pixel of a particle image can be described by a vector $\boldsymbol{p}(k, l)$, where k and l are the discrete coordinates of the pixel and $\|\boldsymbol{p}\|$ is the intensity level. Any given pixel $\boldsymbol{p}_0$ is considered a probable particle centroid peak provided the following two conditions are verified

$$\sum_{k=1}^{w}\sum_{l=1}^{w} U\,[\|\boldsymbol{p}_0\| - \|\boldsymbol{p}(k,l)\|] = \kappa w^2$$
$$\|\boldsymbol{p}_0\| - \min_{k,l}\|\boldsymbol{p}(k,l)\| \geqslant S \tag{15}$$
$$\text{with } U(p) = \begin{cases} 1 & p \geqslant 0 \\ 0 & \text{otherwise} \end{cases}$$

where U is the unit step function, S is a threshold parameter and w defines the size of the window centred on $\boldsymbol{p}_0$. $\kappa \in [0, 1]$ is introduced to account for the overlapping of particle images proper to high density particle fields.

In a third stage, the particle models are built upon contiguous regions of pixels called support sets, following a recursive set-growing routine. Starting on every local peak, the growth continues asymmetrically, until the local intensity gradient reaches a defined threshold. The support sets are then fitted by a 2D Gaussian function, assumed to describe the particle intensity profile (Huang *et al* 1997) and defined by

$$g_i(x, y) = a_i\,\exp\left[\frac{(x-x_{c_i})^2+(y-y_{c_i})^2}{2\,r_i^2}\right] \tag{16}$$

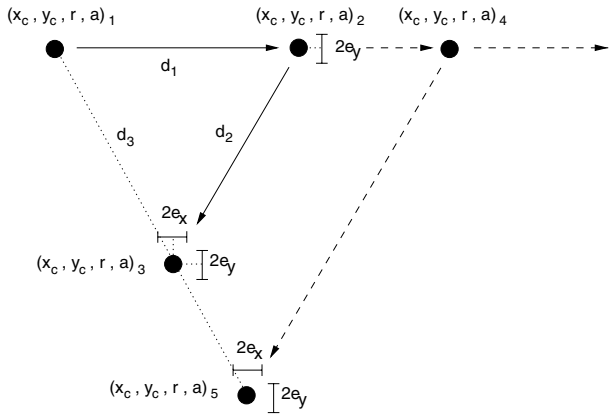

Figure 7. Particle image matching.

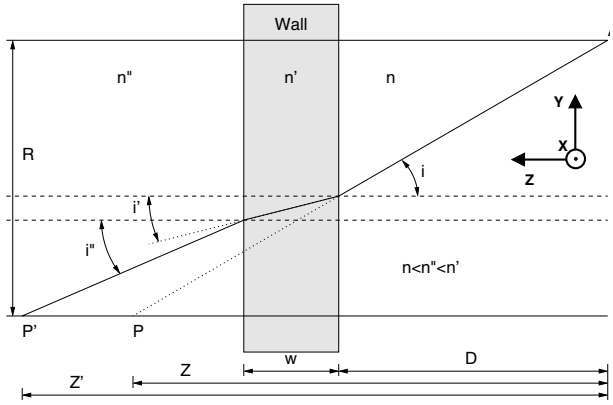

Figure 8. Multimedia optical correction.

where a_i is the amplitude of particle image i, and (x_{c_i}, y_{c_i}) are the subpixel coordinates of the particle image centroid. r_i is the particle image radius and is taken as the standard deviation term of the Gaussian function. These four parameters are optimized by least-squares error minimization.

In a fourth stage, the particle images are tracked to match a given pattern. In the case of apertures arranged in a triangular pattern as used by Pereira *et al* (2000), the search for matching particle images is performed through five conditional steps, illustrated in figure 7 and sequenced as follows

$$\begin{aligned}
&\text{(i)} && |y_{c_2} - y_{c_1}| \leqslant \varepsilon_y \\
&\text{(ii)} && \left| x_{c_3} - \frac{x_{c_1} + x_{c_2}}{2} \right| \leqslant \varepsilon_x \\
&\text{(iii)} && \left| y_{c_3} - \frac{y_{c_1} + y_{c_2}}{2} - \frac{\sqrt{3}}{2} |x_{c_2} - x_{c_1}| \right| \leqslant \varepsilon_y \\
&\text{(iv)} && \left| \frac{r_i - r_j}{r_i} \right| \leqslant \varepsilon_r \qquad \text{with } i, j = 1, 2, 3 \\
&\text{(v)} && \left| \frac{a_i - a_j}{a_i} \right| \leqslant \varepsilon_a
\end{aligned} \tag{17}$$

where ε_ζ is a tolerance coefficient on the variable ζ. A case of a resolved matching ambiguity is also illustrated in figure 7, where the particle image 1 combines with particle images (2, 3) and (4, 5) to form two complete patterns.

In a fifth and final stage, the space coordinates (X, Y, Z) of the particles are calculated following equation (7). For each completed pattern, the separation b and the coordinates (x_0, y_0) are given by the associated set of matched particle images

$$b = \overline{d_i}, \qquad x_0 = \overline{x_{c_i}}, \qquad y_0 = \overline{y_{c_i}} \tag{18}$$

where $\overline{d_i}$ is the average distance between particles in a completed pattern, see figure 7. The particle amplitude and radius are finally computed by

$$A = \overline{a_i}, \qquad R = \frac{1}{M_Z} \left[\overline{r_i} - \frac{\Phi}{2} \left| 1 - \frac{M_Z}{M_p} \right| \right] \tag{19}$$

where Φ is the diameter of an aperture and M_p is defined by $f/(Z - f)$ ($M_p = M_Z = M$ for $Z = L$).

3.2. Multimedia optical correction

The refraction of a light ray passing through a boundary between two media with refractive indices n and n' is described in geometrical optics by the Snell's law $n \sin i = n' \sin i'$, where i is the angle between the incident ray and the normal to the boundary at the point of incidence, and i' is the angle between this normal and the refracted ray. We consider the practical case where the interrogation volume is composed of a medium with refractive index n'', and the DDPIV system is in a medium of index n, see figure 8. Both media are separated by a wall of thickness w and of index n', and the lens–aperture plane of the DDPIV instrument is placed at a distance D from and parallel to the front face of the wall.

The true depth position Z' is a function of the measured coordinates (X, Y, Z) of P:

$$\begin{aligned}
Z' &= D + w + \left[Z - D - \frac{w}{\Omega(n')} \right] \times \Omega(n'') \\
\text{with } \Omega(\nu) &= \sqrt{\frac{R^2}{Z^2} \left[\left(\frac{\nu}{n} \right)^2 - 1 \right] + \left(\frac{\nu}{n} \right)^2} \\
&\text{and } R^2 = X^2 + Y^2.
\end{aligned} \tag{20}$$

3.3. Numerical assessment of location errors

The accuracy of a parameter estimate can be characterized by the root-mean-square (RMS) error

$$\begin{aligned}
\mathrm{RMS}[\varphi] &= \sqrt{E\{(\hat{\varphi} - \varphi)^2\}} \\
&= \sqrt{\mathrm{var}[\hat{\varphi}] + \beta^2[\hat{\varphi}]} \\
\text{with } \mathrm{var}[\hat{\varphi}] &= E\{(\hat{\varphi} - E\{\hat{\varphi}\})^2\} = \sigma^2[\hat{\varphi}] \\
\beta^2[\hat{\varphi}] &= E\{(E\{\hat{\varphi}\} - \varphi)^2\}
\end{aligned} \tag{21}$$

where $\hat{\varphi}$ is an estimator of φ and E is the expected value of the corresponding random variable. $\mathrm{var}[\hat{\varphi}]$ is the variance term that describes the random portion of the error, and $\beta^2[\hat{\varphi}]$ is the square of a bias term that describes the systematic portion of the error. $\sigma[\hat{\varphi}]$ is known as the standard error or standard deviation.

A study of these errors is performed on the basis of synthetic images of particles, generated using the same geometric parameters as in the previous sections: $L = 1000$ mm, $d = 100$ mm. The pinhole diameter Φ is set to 2 mm. The interrogation domain is reduced to a square plane normal to the Z-axis, with side $c = 100$ mm. This plane

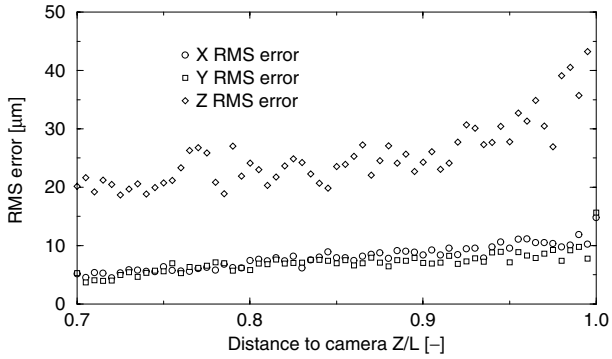

Figure 9. Particle location root-mean-square error.

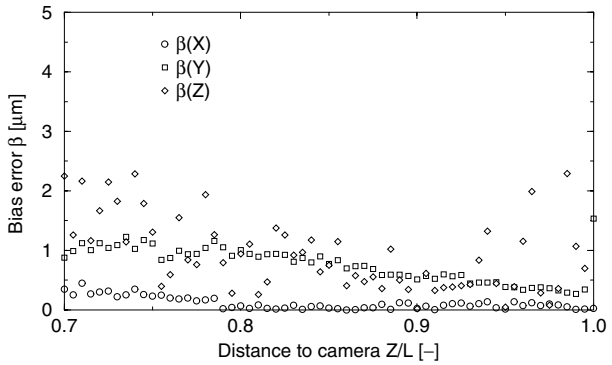

Figure 10. Particle location bias error β.

is seeded with 3000 spatially randomly distributed particles and is shifted along the Z-axis in steps of 5 mm from the reference plane at $Z/L = 1$ to $Z/L = 0.7$. For each Z-station, the particle images are generated as if produced by a three-aperture defocusing system (Pereira *et al* 2000) with a 1024 × 1024-pixel sensor. The image coordinates (x_c, y_c) are derived from the known space coordinates (X, Y, Z) using equations (2). A particle image is then built at each centre (x_c, y_c) using the Gaussian function of equation (16). Applying the particle detection procedures described above to these synthetic images, the calculated space coordinates are then compared with the actual values.

The RMS error and the bias error β on the coordinates (X, Y, Z) are reported in figures 9 and 10, respectively. The RMS errors on X and Y decrease with Z due to their linear dependence upon the depth coordinate, see equations (12). The RMS error on Z shows a power-law trend in agreement with the quadratic dependence on the depth Z reported in equations (12). The systematic error represented by the bias error in figure 10 is found to increase with decreasing Z. This result is explained by the fact that the local magnification M_Z, as defined by equation (3), is inversely proportional to Z, thus amplifying the global systematic error initially present at the reference plane.

The uncertainty Δx on the image plane coordinates (x, y) can be estimated using the definition of $\delta(\mathrm{d}Z)$ from equations (12). Δx is computed using the RMS error on Z and is converted into pixel units, assuming that a pixel is a square of side 10 μm (typical for a CCD sensor). The image uncertainty Δx displayed in figure 11 is contained between 0.015 and 0.025 pixel and is found to be fairly uniform over

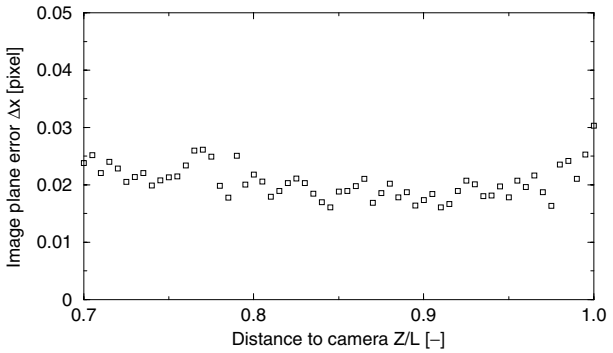

Figure 11. Particle location pixel error.

the whole working volume: the assumption of equation (11) is verified as a consequence of the small aperture diameter Φ.

The basic computer model used here does not constitute a full error analysis, as it does not include any sort of noise sources, such as the shot noise inherent to any photon detection process, the readout noise of the sensor or the errors from the intensity quantization. Various authors (see, for example, Westerweel 1997) have addressed some of these issues, which are beyond the goal of this work.

4. Particle spatial distribution

Our purpose here is to perform a parametric study to determine the limitations of the DDPIV technique in terms of number density and, consequently, of void fraction. We define the particle number density ρ_0 and the void fraction α_0 by

$$\rho_0 = \frac{\int \phi(a)\,\mathrm{d}a}{V_0}, \qquad \alpha_0 = \frac{\int \phi(a)\upsilon(a)\mathrm{d}a}{V_0} \tag{22}$$

where $\phi(a)$ is the probability density function of particles with radius a, V_0 is the observation volume and $\upsilon(a)$ is the sphere volume associated with radius a.

We also define the probability $p(a)$ to find a neighbour particle at a distance d_0 by

$$p(a) = \rho_0 \cdot \delta(a - d_0) \qquad \text{with } \delta(a - d_0) = \begin{cases} 1 & \text{if } d_0 = a \\ 0 & \text{otherwise} \end{cases} \tag{23}$$

where d_0 is the mean particle distance and δ is the Dirac operator. The mean distances $d_{0,2\mathrm{D}}$ and $d_{0,3\mathrm{D}}$, corresponding to the respective probabilities of finding one single particle within a disc and within a sphere, are given after integration of equation (23) by

$$d_{0,2\mathrm{D}} = \sqrt{\frac{1}{\pi\rho_{0,2D}}}, \qquad d_{0,3\mathrm{D}} = \sqrt[3]{\frac{3}{4\pi\rho_{0,3\mathrm{D}}}}. \tag{24}$$

Therefore, for a cubic domain and a square area, both with sidelength c and containing the same number N_0 of particles, we have

$$\frac{d_{0,3\mathrm{D}}}{d_{0,2\mathrm{D}}} \approx N_0^{\frac{1}{6}}. \tag{25}$$

Synthetic images of particles are generated using the same procedure as before. We consider five monodisperse mixtures

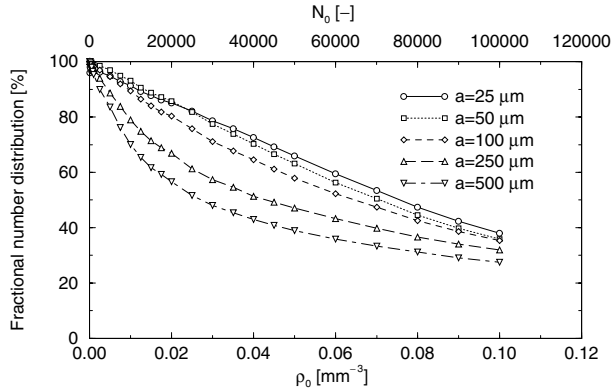

Figure 12. Measured fractional number distribution versus the reference number density for different particle radii.

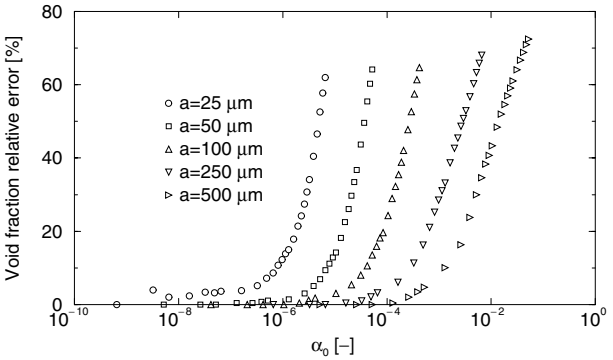

Figure 13. Relative error on the void fraction measurement versus the reference void fraction for different particle radii.

with the following radii: 25, 50, 100, 250 and 500 μm. The number density ρ_0 is varied between 10^{-5} and 10^{-1}, corresponding to particle populations N_0 between 10 and 10^5, respectively. The particles have a zero standard deviation on the radius and are spatially randomly distributed inside a cubic domain with sidelength $c = 100$ mm. Figure 12 represents the measured relative number density as a function of the actual number density ρ_0, or conversely as a function of the actual population N_0. The plot points to a loss of particles in the search process due to the overcrowding which translates into a screening effect, and the consequent overlapping of particle images. This effect worsens for a larger number density and/or a larger radius. For $\rho_0 = 10^{-2}$ ($N_0 = 10^4$), we find 93% of the actual particle population for a radius $a = 50$ μm and only 70% for $a = 500$ μm. The rate of loss of particles is higher for increased radius, with a closely linear trend for $a < 100$ μm.

In terms of void fraction measurement, figure 13 shows that α_0 is estimated with an error less than 10% for void fractions up to $\approx 10^{-3}$ for $a = 500$ μm and up to $\approx 10^{-5}$ for $a = 50$ μm.

Because high void fractions unavoidably yield to particle occlusion, as observed above, the performance of a DDPIV system can be improved by reducing the depth of the interrogation volume and/or by increasing the pixel resolution of the sensor, i.e. the number of pixels per length unit. Alternatively, a special optical arrangement as proposed by Pereira *et al* (2000), and successfully applied to a high density bubbly flow in a $300 \times 300 \times 300$ mm^3 volume, can be implemented.

5. Velocity estimation

5.1. The particle field

Let $\boldsymbol{P}(X, Y, Z)$ be the position vector in the Cartesian 3D space. For conciseness, $\boldsymbol{P}(X, Y, Z)$ will be written as $\boldsymbol{P}$. We describe an ensemble of particles, at time t, by a random process $\underline{\boldsymbol{F}}(\boldsymbol{P}, t)$

$$\underline{\boldsymbol{F}}(\boldsymbol{P}, t) = \sum h(\boldsymbol{P} - \boldsymbol{P}_i, t). \tag{26}$$

Equation (26) represents a sum of functions resulting by shifting $h(\boldsymbol{P}, t)$ by the random position $\boldsymbol{P}_i$. Thus, the process $\underline{\boldsymbol{F}}(\boldsymbol{P}, t)$ can be interpreted as the output of a linear system with input $\underline{\boldsymbol{Z}}(\boldsymbol{P}, t)$ and impulse response $h(\boldsymbol{P}, t)$

$$\begin{aligned} &\underline{\boldsymbol{F}}(\boldsymbol{P}, t) = \underline{\boldsymbol{Z}}(\boldsymbol{P}, t) * h(\boldsymbol{P}, t) \\ &\text{with } \underline{\boldsymbol{Z}}(\boldsymbol{P}, t) = \sum_i \delta(\boldsymbol{P} - \boldsymbol{P}_i, t) \end{aligned} \tag{27}$$

where $*$ is the convolution operator and δ is the Dirac δ-function. $\underline{\boldsymbol{Z}}(\boldsymbol{P}, t)$ describes a stochastic process known as 'Poisson impulses', defined by

$$\underline{\boldsymbol{Z}}(\boldsymbol{P}, t) = \lim_{D \to 0} \underline{\boldsymbol{Y}}(\boldsymbol{P}, t) \tag{28}$$

where $\underline{\boldsymbol{Y}}(\boldsymbol{P}, t)$ equals the number of particles in the volume domain $\boldsymbol{D}$ defined by $[\boldsymbol{P}, \boldsymbol{P} + \boldsymbol{D}]$, with $\boldsymbol{D}$ being the spatial shift or displacement of the particle field. $\underline{\boldsymbol{Y}}(\boldsymbol{P}, t)$ is a Poisson process for which the probability to have k particles in the volume domain $\boldsymbol{D}$ is given by

$$\text{prob}\left\{ \|\underline{\boldsymbol{Y}}(\boldsymbol{P}, t)\| = \frac{k}{D} \right\} = \mathrm{e}^{-\lambda D} \frac{(\lambda D)^k}{k!} \qquad \text{with } D = \|\boldsymbol{D}\| \tag{29}$$

where λD is the parameter of the distribution, with λ being the particle density. Based on this description, the particle field $\underline{\boldsymbol{F}}(\boldsymbol{P}, t)$ can be interpreted as equivalent to a 'shot noise' process.

5.2. Displacement evaluation methodology

The particle displacement in standard PIV analysis has been evaluated for a long time through autocorrelation, until imaging devices have become available to take separate images of the particle field at very short intervals of time (Adrian 1991, Willert and Gharib 1991). In modern DPIV, the displacement is evaluated through a window-based cross-correlation performed in the image pixel space. The correctness of the estimate of the displacement vector depends essentially on the accurate detection of the correlation peak. The first implementations were based on integer pixel schemes implying resolutions of ± 0.5 pixel (Kimura and Takamori 1986). Nowadays, subpixel accuracies of the order of 1/10th to 1/20th are common using different peak finding algorithms (Lourenco and Krothapalli 1995).

In the DDPIV technique, the displacement is estimated by performing a 3D spatial cross-correlation of particle locations,

i.e. in the physical space of the particle field and not in the discrete pixel image space as in PIV. Let $\underline{\boldsymbol{F}}'$ and $\underline{\boldsymbol{F}}''$ be two particle fields sampled at two instances t' and t'':

$$\begin{aligned} \underline{\boldsymbol{F}}' &= \underline{\boldsymbol{F}}(\boldsymbol{P}', t') \\ \underline{\boldsymbol{F}}'' &= \underline{\boldsymbol{F}}(\boldsymbol{P}'', t'') = \underline{\boldsymbol{F}}(\boldsymbol{P}', t') * \delta(\boldsymbol{P}'' - \boldsymbol{P}' - \boldsymbol{D}). \end{aligned} \tag{30}$$

The particle field $\underline{\boldsymbol{F}}''$ is the shift of $\underline{\boldsymbol{F}}'$ by the local displacement $\boldsymbol{D}$. $\boldsymbol{P}'$ and $\boldsymbol{P}''$ are the particle descriptors at instants t' and t'', respectively.

We suppose that the displacement $\boldsymbol{D}$ is uniform, that no particles are either introduced or removed between instants t' and t'', and that the density λ is uniform (i.e. the seeding is homogeneous). Using Campbell's theorem regarding conditional probabilities, the mean values $\mu_{\underline{\boldsymbol{F}}'}$ and $\mu_{\underline{\boldsymbol{F}}''}$, the cross-correlation $R_{\underline{\boldsymbol{F}}'\underline{\boldsymbol{F}}''}$ and the cross-covariance $C_{\underline{\boldsymbol{F}}'\underline{\boldsymbol{F}}''}$ are expressed by

$$\begin{aligned} \mu_{\underline{\boldsymbol{F}}'} &= E\{\underline{\boldsymbol{F}}'\} = E\{\underline{\boldsymbol{Z}}(\boldsymbol{P}', t')\} \int h(\boldsymbol{\Pi}, t')\, \mathrm{d}\boldsymbol{\Pi} \\ &= \lambda \int h(\boldsymbol{\Pi}, t')\, \mathrm{d}\boldsymbol{\Pi} \\ \mu_{\underline{\boldsymbol{F}}''} &= E\{\underline{\boldsymbol{F}}''\} = \lambda \int h(\boldsymbol{\Pi}, t'')\, \mathrm{d}\boldsymbol{\Pi} \\ R_{\underline{\boldsymbol{F}}'\underline{\boldsymbol{F}}''} &= E\{\underline{\boldsymbol{F}}'\underline{\boldsymbol{F}}''\} \\ &= \int \underline{\boldsymbol{F}}'\underline{\boldsymbol{F}}'' \mathrm{prob}(\underline{\boldsymbol{F}}')\mathrm{prob}(\underline{\boldsymbol{F}}''|\underline{\boldsymbol{F}}')\, \mathrm{d}\boldsymbol{\Pi} \\ &= \lambda^2 \int h(\boldsymbol{\Pi}, t')\, \mathrm{d}\boldsymbol{\Pi} \int h(\boldsymbol{\Pi}, t'')\, \mathrm{d}\boldsymbol{\Pi} \\ &\quad + \lambda \int h(\boldsymbol{\Pi}, t') h(\boldsymbol{\Pi} - \boldsymbol{D}, t'')\, \mathrm{d}\boldsymbol{\Pi} \\ C_{\underline{\boldsymbol{F}}'\underline{\boldsymbol{F}}''} &= R_{\underline{\boldsymbol{F}}'\underline{\boldsymbol{F}}''} - E\{\underline{\boldsymbol{F}}'\}E\{\underline{\boldsymbol{F}}''\} \\ &= \lambda \int h(\boldsymbol{\Pi}, t') h(\boldsymbol{\Pi} - \boldsymbol{D}, t'')\, \mathrm{d}\boldsymbol{\Pi} \end{aligned} \tag{31}$$

where $E\{\zeta\}$ is the expected value of a variable ζ.

5.3. Computational implementation

We assume that we have two particle ensembles $\underline{\boldsymbol{F}}'$ and $\underline{\boldsymbol{F}}''$. The flow domain is divided into contiguous elements of volume, or 'voxels'. A voxel is a small cell relative to which flow computations are done. Each voxel is a rectangular solid, with edges parallel to the coordinate axes, and is defined by a centre and its size along each axis. Voxels are distributed on a regular lattice that encompasses the domain of interest of the flow.

For each voxel, the flow velocity estimate is computed. A subset $\underline{\boldsymbol{f}}'$ is extracted from the first ensemble $\underline{\boldsymbol{F}}'$, such that the particles of this subset are spatially located inside the voxel under consideration. A second subset $\underline{\boldsymbol{f}}''$ is collected from $\underline{\boldsymbol{F}}''$ that verifies the same condition. A cross-correlation between these two subsets of particles is computed following the relation of equation (31). To perform this operation, we assume that the impulse response h of a particle is represented by an isotropic 3D Gaussian function

$$\begin{aligned} &G_i(X, Y, Z) \\ &= A_i \exp\left[-\frac{(X - X_{c_i})^2 + (Y - Y_{c_i})^2 + (Z - Z_{c_i})^2}{2\, R_i^2} \right] \end{aligned} \tag{32}$$

where the amplitude A_i, the radius R_i and the centroid 3D coordinates $(X_{c_i}, Y_{c_i}, Z_{c_i})$ of particle i are taken from equations (7), (18) and (19).

The convolution of two Gaussian functions is itself a Gaussian function. Therefore, the cross-correlation of two particles G_i and G_j, taken respectively from subsets $\underline{\boldsymbol{f}}'$ and $\underline{\boldsymbol{f}}''$, would be

$$\begin{aligned} R_{G_i,G_j} &= A_i A_j \left(\frac{\sqrt{2\pi} R_i R_j}{\sqrt{R_i^2 + R_j^2}} \right)^3 \\ &\quad \times \exp\left[-\frac{1}{2} \frac{(X + X_i - X_j)^2 + (Y + Y_i - Y_j)^2}{R_i^2 + R_j^2} \right. \\ &\quad \left. - \frac{1}{2} \frac{(Z + Z_i - Z_j)^2}{R_i^2 + R_j^2} \right]. \end{aligned} \tag{33}$$

However, in order to preserve the concept of the matching of particles between two consecutive subsets, we replace the amplitude factor in equation (33) by an amplitude function defined by

$$A_{ij} = \exp\left[-\chi (R_i - R_j) \right] \tag{34}$$

where χ is a positive factor. Hence, we penalize the cross-correlation for R_i being different from R_j.

A truncated Newton optimizer is used to find the maximum of the cross-correlation function R_{G_i,G_j}. The 3D location of this maximum is interpreted as the displacement of the flow at the centre of the voxel being processed; the displacement divided by $(t''-t')$ is the flow velocity estimate at this location. The 3D correlation is finally refined using a voxel offset procedure similar to the window offset method used in classical DPIV. Initially proposed by Keane and Adrian (1992) and later extended to DPIV by Westerweel *et al* (1997), this technique, now standard in PIV applications, improves the estimation of the displacement-correlation peak. In the case of DDPIV, the 'refined' flow velocity estimate is performed as for the initial estimate, except that the position of the voxel for $\underline{\boldsymbol{f}}''$ is offset from the voxel position for $\underline{\boldsymbol{f}}'$ by the recently obtained estimate of the flow displacement.

5.4. Numerical assessment of displacement errors

One of the research trends in recent years in the field of PIV has been to locate the sources of errors linked to the computation of the velocity vectors.

Outliers are velocity vectors that are incorrectly determined, due to poor correlation. These invalid vectors appear with random direction and norm, unphysically deviating from the surrounding vector neighbours. They are more likely to appear with complex flows, especially where strong velocity gradients and/or three-dimensionality exist. Low or non-uniform seeding density is also a main factor in generating outliers due to the higher probability of obtaining unpaired particles. These many causes generate random, distorted and misplaced correlation peaks that are either difficult to fit using the standard models or are indistinct from the surrounding peaks. Methods have been developed for planar PIV to reduce and correct these so-called spurious vectors. Detailed studies are available on this subject (Keane and Adrian 1990, Westerweel 1994). Most of these methods rely on the accuracy or similarity of neighbouring vectors;

Table 1. Displacement error calculations: (ρ_0, υ) cases.

Particle density ρ_0 (mm^{-3})	Particle number N_0 —	Particle number per voxel volume υ (mm^3) 7.5^3 (υ_0)	10^3 (υ_1)	12.5^3 (υ_2)	15^3 (υ_3)
5×10^{-3}	5 000	—	—	9.77	—
10×10^{-3}	10 000	4.22	10	19.53	33.75
25×10^{-3}	25 000	—	—	48.83	—

though, non-post-interrogation approaches have also been reported (Hart 2000). Errors are also present in the valid velocity vectors, i.e. obtained with large correlation peaks, and are essentially of two types: mean-bias and RMS. These errors result generally from the correlation computation (Huang *et al* 1997) or from the peak-finding schemes used to extract the peak of the correlation function (Lourenco and Krothapalli 1995).

The spatial correlation performed in DDPIV differs from the pixel-based correlation computed in standard PIV techniques. However, outliers, bias and mean errors still exist for the same reasons. Our purpose here is to analyse the global error on the displacement evaluation as a function of the particle number density ρ_0 and of the voxel size υ. Synthetic particle data fields are generated following the same procedure used previously, with unchanged geometrical parameters: $L = 1000$ mm, $d = 100$ mm. The particle radius a is set to 50 μm with a zero standard deviation. Table 1 lists the six sets (ρ_0, υ) considered in the simulations. For each case, the synthetic particle data set occupies a cubic domain with sidelength $c = 100$ mm and is translated successively in each spatial direction from 0 to 5 mm in steps of 100 μm. A 50% overlap between adjacent voxels of the vector lattice is used and the voxel shift technique is applied to compute the refined 3D velocity field. No correction (i.e. outlier removal) is applied to the calculated velocity field.

We define the normalized standard error ε_s on the displacement variables ΔX, ΔY and ΔZ following the same definitions of equation (21). ε_s is voxel-averaged over the entire interrogation domain. Figure 14 represents ε_s for each axis as a function of the voxel size and for a constant particle density $\rho_0 = 10^{-2}$ ($N_0 = 10^4$). The results for X and Y show similar features pointing out to the outliers as the predominant source of error: the errors are essentially dependent upon the number of particles common to subsets $\underline{f}'$ and $\underline{f}''$. The theoretical number of such particles is given by

$$n_0 = \upsilon' \rho_0 \exp\left[-\frac{1}{2}\frac{(\rho - \rho_0)^2}{\sigma_\rho^2}\right] \qquad (35)$$

$$\text{with } \upsilon' = (\delta - |\Delta X|)(\delta - |\Delta Y|)(\delta - |\Delta Z|)$$

where $\delta = \upsilon^{\frac{1}{3}}$ is the sidelength of a voxel and σ_ρ is the standard deviation on the input number density.

The ε_s curves for υ_1 give an indication of the minimum number of pairs before the error level increases: ε_s is found to markedly increase for $\Delta X > 3$ mm, the same observation holding for $\Delta Y > 4$ mm. The corresponding number of common particles is $n_0 = 7$. The curve for υ_0 does not show such a limit because the maximum number of particles

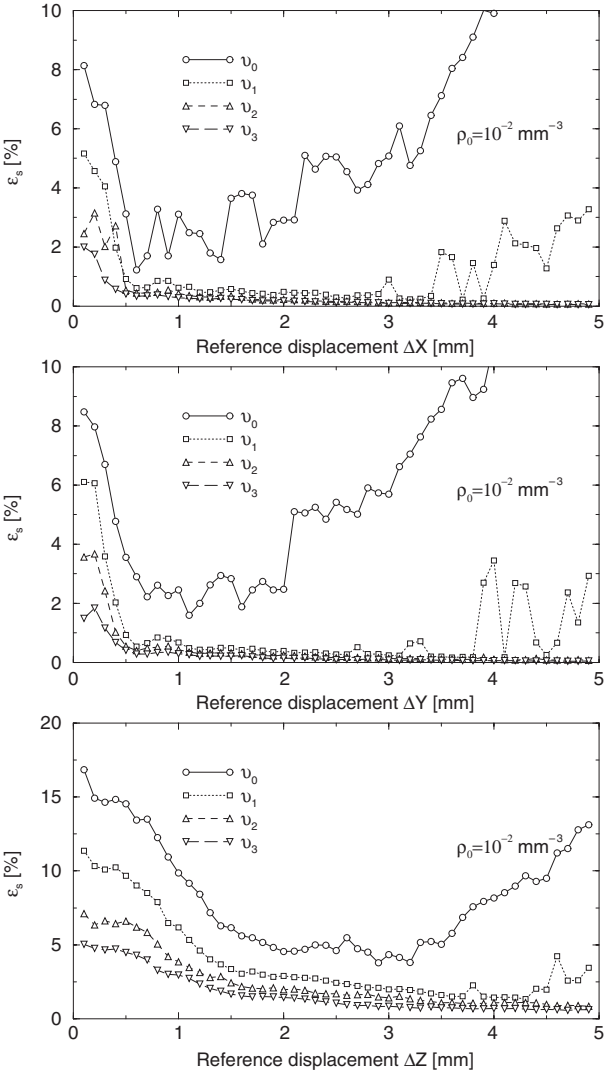

Figure 14. Normalized standard error ε_s at constant ρ_0 on the X (top), Y (centre) and Z (bottom) displacements. Refer to table 1 for the values of υ_0, υ_1, υ_2 and υ_3.

in a voxel is only 4.22, see table 1. For υ_2 and υ_3, this limit would only appear for ΔX or ΔY larger than 8 and 12 mm, respectively. Within these limits, the levels are below 1% for υ_1 and under 0.5% for υ_2 and υ_3.

The same plots show another common feature: ε_s is found to increase steeply for displacements less than 0.5 mm. This sudden increase is a bias error introduced by the overlapping of particle images. From equations (24), the mean distance between particles is $d_{0,3D} \approx 2.88$ mm. This corresponds, on the image, to an apparent distance between particles of $d_{0,2D} \approx 0.620$ mm, see equation (25). $d_{0,2D}$ matches the value of the displacement threshold found on the plots and corresponds to a mean distance of 5.1 pixels on the image plane. This distance corresponds to a non-overlapping situation for a 5×5 pixel kernel, the size used here for the peak finding procedure described by equations (15). Allowance for overlapping (i.e. for an overlapping factor $\kappa \in]0, 1]$) naturally introduces a bias into the determination of the peak subpixel coordinates and therefore into the particle displacements (ΔX, ΔY).

The curves for the displacement ΔZ show a lower bound threshold visible around $\Delta Z \approx 1.2$ mm, derived from the overlapping occurrence discussed before. However, the value is more than doubled since the depth component is calculated from the image separation b. The upper threshold follows from the same reasons as for the X and Y displacements. Within these boundaries, ε_s is under 4%. $\varepsilon_s[Z]$ is approximately four to six times higher than $\varepsilon_s[X]$ and $\varepsilon_s[Y]$, which is in good agreement with the simulation results of figure 9.

Figure 15 represents ε_s for each direction of displacement as a function of the particle density ρ_0 and for a constant voxel size $\upsilon = \upsilon_2$ ($\delta = 12.5$ mm). The displacement threshold at approximately 0.5 mm is not significantly changed when increasing the particle density. Instead, a negative effect on the RMS error can be generally observed, especially on the X and Y displacements, for the percentage of detected particles is truncated by 3% for $\rho_0 = 5 \times 10^{-3}$ and by 18% for $\rho_0 = 25 \times 10^{-3}$, see figure 12. As we have already pointed out, the errors would improve with a smaller volume depth and/or with a higher image spatial resolution. Yet, the error ε_s remains below 1% for X and Y for $\rho_0 = 25 \times 10^{-3}$, while the error on Z is little influenced by density changes and remains under 4% for $\Delta Z > 1.2$.

6. Conclusion

DDPIV is the extension of planar digital PIV to the third dimension. DDPIV uses an original optical concept combined with remodelled digital PIV methodologies to produce a true whole field velocity measurement technique. Hence, DDPIV brings standard PIV into the restricted class of 3D measurement methods for fluid mechanical research.

The technique is primarily devised to provide a measure of the 3D coordinates of light scatterers, such as flow markers or bubbles, in a similar way to the PTV approach. However, unlike PTV methods, DDPIV has one unique optical axis that simplifies drastically its implementation in all aspects from the experimental set-up to the data processing. Moreover, and to address the important issue of particle density limits associated with 3D measurements, DDPIV is intended to map particle densities extending from the low range required for PTV tracking procedures to the high particle numbers used in PIV methods. The upper limit depends essentially upon two parameters:

(1) the size of the 3D interrogation domain;
(2) the resolution of the recording sensor.

The geometrical and optical characteristics of a DDPIV system have been laid out. To establish the DDPIV performance, we carried out an uncertainty study based on a system of practical interest. The particle coordinates have been determined with an average RMS error equivalent to 0.02 pixel. The performance has been analysed in terms of particle number density and particle size and has shown that the overall performance deteriorates with increasing void fraction. The velocity field calculation within DDPIV integrates the concepts of standard PIV. In particular, the evaluation of the particle displacement is done through the correlation method. However, unlike the pixel window correlation technique used in most planar PIV techniques, the DDPIV correlation is

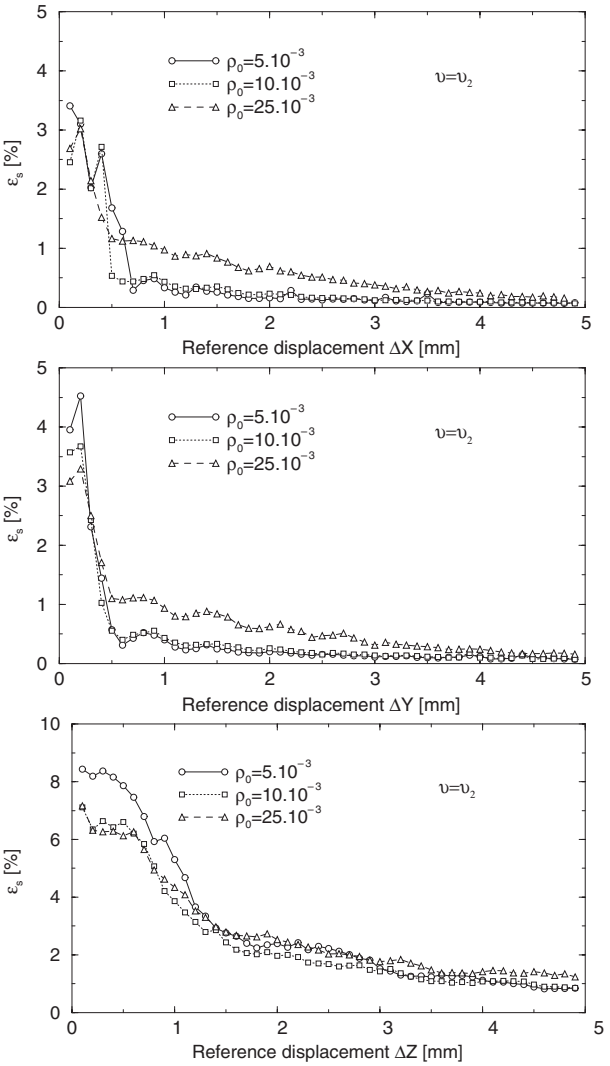

Figure 15. Normalized standard error ε_s at constant voxel volume υ on the X (top), Y (centre) and Z (bottom) displacements.

performed in the spatial 3D domain using the particle size and 3D coordinates. An equivalent of the window offset procedure has been implemented to improve the correlation levels between volume elements containing time-separated subsets of particles. Such volume elements, or voxels, are the 3D counterpart of the correlation windows in the image space for standard PIV. A normalized standard error of less than 1% has been established for the X and Y displacements, whereas the error on the depth displacement is four to six times higher. A number of seven pairs per voxel seemed to be a minimum requirement to maintain the low error over a range of displacements.

In practice, errors in particle location and displacement can be improved by the adjustment of the size of the interrogation volume, specifically the depth, to the actual particle field situation. Alternatively, higher spatial resolution recording sensors can be used to extend the potential of a given DDPIV system.

DDPIV, as per its flexibility and simplicity of implementation, is foreseen to be an ideal instrument for a broad range of problems in the field of experimental fluid

mechanics, with a level of performance ranging from PTV to planar PIV.

Acknowledgments

The visit of Dr F Pereira to the CQV was made possible by a fellowship of the *Fundação para a Ciência e a Tecnologia*, Portugal. The research was supported by the Office of Naval Research (contract N00014-97-1-0303), under the direction of Dr Ed P Rood and Dr Mark Hyman. The DDPIV technology is protected under a US pending patent filed by the California Institute of Technology.

References

Abe M, Yoshida N, Hishida K and Maeda M 1998 Multilayer PIV technique with high power pulse laser diodes *Proc. 9th Int. Symp. on Appl. Laser Tech. Fluid Mech.* (Lisbon, Portugal: Instituto Superior Técnico)

Adrian R J 1986 Multi-point optical measurements of simultaneous vectors in unsteady flow—a review *Int. J. Heat Fluid Flow* **7** 127–45

Adrian R J 1991 Particle-Imaging techniques for experimental fluid mechanics *Annu. Rev. Fluid Mech.* **23** 261–304

Agüí J C and Jiménez J 1987 On the performance of particle tracking *J. Fluid Mech.* **185** 447–68

Brücker C 1997 3D Scanning PIV applied to an air flow in a motored engine using digital high-speed video *Meas. Sci. Technol.* **8** 1480–92

Cho Y C 1989 Digital image velocimetry *Appl. Opt.* **28** 740–8

Gauthier V and Riethmuller M L 1988 Application of PIDV to complex flows: measurements of the third component Von Kármán institute for fluid mechanics *Particle Image Displacement Velocimetry* (Belgium: Rhode-Saint-Genèse)

Gharib M, Hernan M A, Yavrouian A H and Sarohia V 1985 Flow velocity measurement by image processing of optically activated tracers *AIAA Paper* 85–0172

Grant I, Fu S, Pan X and Wang X 1995 The application of an in-line, stereoscopic, PIV system to 3-component velocity measurements *Exp. Fluids* **19** 214–21

Green S I and Zhao Z 1994 Reconstructed double-pulsed holograms: a system for efficient automated analysis *Appl. Opt.* **33** 761–7

Hart D P 2000 PIV error correction *Exp. Fluids* **29** 1–12

Higuchi H, Lewalle J and Crane P 1994 On the structure of a two-dimensional wake behind a pair of flat plates *Phys. Fluids* A **6** 297–305

Huang H, Dabiri D and Gharib M 1997 On errors of digital particle image velocimetry *Meas. Sci. Technol.* **8** 1427–40

Kähler C J and Kompenhans J 2000 Fundamentals of multiple plane stereo particle image velocimetry *Exp. Fluids* **29** S070–7

Katz J, Gowing S, O'Hern T and Acosta A 1983 A comparative study between holographic and light-scattering techniques of microbubble detection *Proc. Symp. Measuring Techniques in Gas-Liquid Two-Phase Flows* (Nancy, France: IUTAM) pp 41–66

Keane R D and Adrian R J 1990 Optimization of particle image velocimeters: part i. Double pulsed systems *Meas. Sci. Technol.* **1** 1202–15

Keane R D and Adrian R J 1992 Theory of cross-correlation analysis of PIV images *Appl. Sci. Res.* **49** 191–215

Kimura I and Takamori T 1986 Image processing of flow around a circular cylinder by using correlation technique *Flow Visualization* vol 4 (Washington: Hemisphere) pp 221–6

Lee S J, Chung M K, Mun C W and Cho Z H 1987 Experimental study of thermally stratified unsteady flow by NMR-CT *Exp. Fluids* **5** 787–802

Lourenco L and Krothapalli A 1995 On the accuracy of velocity and vorticity measurements with PIV *Exp. Fluids* **18** 421–8

Malik N A and Dracos T 1993 Lagrangian PTV in 3D flows *Appl. Sci. Res.* **51** 161–6

Malkiel E, Alquaddoomi O and Katz J 1999 Measurements of plankton distribution in the ocean using submersible holography *Meas. Sci. Technol.* **10** 1142–52

Meynart R 1983 Instantaneous velocity field measurements in unsteady gas flow by speckle velocimetry *Appl. Opt.* **22** 535–40

Miles R B, Connors J J, Markovitz E C, Howard P J and Roth G J 1989 Instantaneous profiles and turbulence statistics of supersonic free shear layers by Raman excitation plus laser induced electronic fluorescence (Relief) velocity tagging of oxygen *Exp. Fluids* **8** 17–24

Murai S, Nakamura H and Suzaki Y 1980 Analytical orientation for non-metric camera in the application to terrestrial photogrammetry *Int. Arch. Photogramm.* **23** 516–25

Nishino K, Kasagi N and Hirata M 1989 Three-dimensional particle tracking velocimetry based on automated digital image processing *J. Fluids Eng.* **111** 384–91

Pereira F, Gharib M, Dabiri D and Modarress D 2000 Defocusing digital particle image velocimetry: a 3-component 3-dimensional DPIV measurement technique. application to bubbly flows *Exp. Fluids* **29** S78–84

Prasad A K and Adrian R J 1993 Stereoscopic particle image velocimetry applied to liquid flows *Exp. Fluids* **15** 49–60

Prasad A K and Jensen K 1995 Scheimpflug stereocamera for particle image velocimetry in liquid flows *Appl. Opt.* **34** 7092–9

Racca R G and Dewey J M 1988 A method for automatic particle tracking in a three-dimensional flow field *Exp. Fluids* **6** 25–32

Raffel M, Westerweel J, Willert C, Gharib M and Kompenhans J 1996 Analytical and experimental investigations of dual-plane particle image velocimetry *Opt. Eng.* **35** 2067–74

Reese J, Chen R C and S F L 1995 Three-dimensional particle image velocimetry for use in three-phase fluidization systems *Exp. Fluids* **19** 367–78

Sheu Y, Chang T and Tatterson G 1982 A Three-dimensional measurement technique for turbulent flows *Chem. Eng. Commun.* **17** 67–83

Soloff S M, Adrian R J and Liu Z C 1997 Distortion compensation for generalized stereoscopic particle image velocimetry *Meas. Sci. Technol.* **8** 1441–54

Westerweel J 1994 Efficient detection of spurious vectors in particle image velocimetry data *Exp. Fluids* **16** 236–47

Westerweel J 1997 Fundamentals of digital particle image velocimetry *Meas. Sci. Technol.* **8** 1379–92

Westerweel J, Dabiri D and Gharib M 1997 The effect of a discrete window offset on the accuracy of cross-correlation analysis of digital PIV recordings *Exp. Fluids* **23** 20–8

Willert C E and Gharib M 1991 Digital particle image velocimetry *Exp. Fluids* **10** 181–93

Willert C E and Gharib M 1992 Three-dimensional particle imaging with a single camera *Exp. Fluids* **12** 353–8

Zhang J, Tao B and Katz J 1997 Turbulent flow measurement in a square duct with hybrid holographic PIV *Exp. Fluids* **23** 373–81